Journal of Advanced Ceramics
2024, **13**(12): 1996–2003
https://doi.org/10.26599/JAC.2024.9220992

Research Article

Brilliant cryogenic magnetic refrigerant with excellent magnetocaloric effect and refrigeration performances

Zhao-Jun Mo[1,†,✉], Hui-Cai Xie[1,2,†], Yan Li[1], Jia-Xin Jiang[1], Zhen-Xing Li[3], Xin-Qiang Gao[1], Feng-Xia Hu[4], Jun Shen[3,✉], Bao-Gen Shen[4]

[1] *Key Laboratory of Rare Earths, Ganjiang Innovation Academy, Chinese Academy of Sciences, Ganzhou 341119, China*
[2] *Jiangxi University of Science and Technology, Ganzhou 341000, China*
[3] *School of Mechanical Engineering, Beijing Institute of Technology, Beijing 100081, China*
[4] *Beijing National Laboratory for Condensed Matter Physics, Institute of Physics, Chinese Academy of Sciences, Beijing 100190, China*

Received: September 6, 2024; Revised: October 5, 2024; Accepted: October 17, 2024

Abstract: There is an urgent demand for the development of new resource-saving and high-efficiency cryogenic refrigeration technologies against the historical backdrop of increasing scarcity of resources and energy. Magnetic refrigeration technology based on the magnetocaloric effect (MCE) of magnetic materials is a promising approach to address helium resource constraints and improve energy efficiency. Here, a brilliant cryogenic magnetic refrigerant with a large low-field MCE and excellent refrigeration performance is presented. Benefiting from the enhanced ferromagnetism and low saturation magnetic field, the peaks of magnetic entropy change, refrigeration capacity, and adiabatic temperature change of $Eu(Ti,Nb,Zr)O_3$ compounds reach 19.6 $J·kg^{-1}·K^{-1}$, 87.6 $J·kg^{-1}$, and 5.5 K, respectively, for a field change of 0−1 T. Magnetic refrigeration experiments on a Gifford–McMahon (GM)/magnetic hybrid refrigerator further demonstrated that $EuTi_{0.8375}Nb_{0.0625}Zr_{0.1}O_3$ is an excellent magnetic refrigerant operating near the liquid helium temperature. An appropriate amount of this magnetic refrigerant can significantly improve the refrigeration performance of the hybrid refrigerator. The cooling power in hybrid refrigeration mode is improved by a maximum of 52% over that in pure GM/$HoCu_2$ mode at 4.2 K and 0.5 Hz. In addition, the cooling efficiency at 4.2 K is more than 40% greater than that of the pure GM/$HoCu_2$ refrigerator.

Keywords: magnetic refrigerant; magnetocaloric effect (MCE); cryogenic refrigeration; Gifford–McMahon (GM)/magnetic hybrid refrigerator

1 Introduction

Cryogenic refrigeration plays an important role in many fields of cutting-edge science and engineering technology and has become one of the most critical technologies for supporting the development of modern science and technology as well as national security [1–3]. In recent years, the demands for cryogenic refrigeration have continuously improved, which is mainly embodied in a greater cooling power, higher efficiency, and lower temperature. However, traditional cryogenic refrigeration technologies suffer from high operational costs because of their low efficiency and high dependence on scarce helium resources [4]. Therefore, there is an urgent need to develop an efficient, resource-saving, and liquid helium-free cryogenic refrigeration technology. Subsequently, a number of new refrigeration technologies have emerged, including semiconductor refrigeration [5], electrocaloric refrigeration [6,7], thermoacoustic refrigeration [8], and magnetic refrigeration [9–11].

Magnetic refrigeration is very attractive in cryogenic refrigeration because of its high intrinsic efficiency and independence of liquid helium, which is considered an excellent alternative to conventional cryogenic refrigeration technology [12–14]. Moreover, magnetic refrigeration has a thermodynamic cycle similar to that of Gifford-McMahon (GM) refrigeration; thus, combining the two technologies is an effective way to improve refrigeration efficiency. Yayama *et al.* [15] proposed a new hybrid cryogenic refrigerator that combines the Brayton magnetic refrigeration cycle and the GM gas refrigeration cycle. They evaluated the cooling power of a hybrid refrigerator with an ErNi regenerator material via numerical simulation and reported that the cooling power was significantly greater than that of a conventional GM refrigerator. Shen *et al.* [16] constructed a hybrid refrigerator that combines the GM cycle with the active magnetic regenerator (AMR) cycle at liquid helium temperature and experimentally demonstrated the feasibility of combining magnetic refrigeration and GM refrigeration. ErNi and TmCuAl with large magnetocaloric effects were used to fill the AMR and yielded a minimal no-load temperature of 3.5 K at 0.5 Hz, which is markedly lower than the temperature (4.2 K) achievable with pure GM refrigeration. Numerical simulations have shown that at 4 K and 0.4 Hz, the cooling power and efficiency of the hybrid refrigerator with ErNi filling are 57% and 68% higher than those of the GM refrigerator, respectively [17]. Superior refrigeration

† Zhao-Jun Mo and Hui-Cai Xie contributed equally to this work.
✉ Corresponding authors.
E-mail: Z.-J. Mo, mozhaojun@gia.cas.cn;
J. Shen, jshen@bit.edu.cn

performance could be achieved by using higher-performance cryogenic magnetic refrigerants, e.g., $EuTi_{0.875}Al_{0.125}O_3$, as the filler of AMR [18]. The cooling power and cooling efficiency reach 0.652 W and 0.48% at 4.2 K and 0.4 Hz, respectively, which are significantly greater than those of the pure GM refrigeration mode. Therefore, researchers in related fields have never stopped pursuing high-performance magnetic refrigeration materials, especially those with large magnetocaloric effects (MCEs) under relatively low magnetic fields (≤ 2 T).

In general, ferromagnetic (FM) materials require a low driving magnetic field and exhibit a large MCE at a low magnetic field, such as TmCuAl [19], TmZn [20], $Er_{1-x}Tm_xAl_2$ [21], and $Eu_2B_2O_5$ [22]. $EuTiO_3$ is a typical antiferromagnetic (AFM) material that has a large MCE at low magnetic fields, with maximum magnetic entropy changes ($-\Delta S_M^{max}$) of 11.0 and 22.3 $J{\cdot}kg^{-1}{\cdot}K^{-1}$ under field changes of 0–1 and 0–2 T, respectively [23]. More interestingly, there is a delicate balance of AFM and FM interactions in $EuTiO_3$ [24], which can be broken by some specific foreign factors and lead to a domination of FM interactions, such as lattice expansion [25], itinerant electrons [26], and biaxial strain [27]. The tunability of the magnetic ground state in $EuTiO_3$ provides the availability of $EuTiO_3$-based materials with large low-field MCEs. In single-crystal $EuTi_{0.85}Nb_{0.15}O_3$, Nb-doping-induced itinerant electrons mediate the FM ordering of localized Eu^{2+} spins so that the spin entropy is strongly suppressed and a giant MCE is observed [28]. The values of $-\Delta S_M^{max}$ and the refrigerating capacity (RC) are 14.7 $J{\cdot}kg^{-1}{\cdot}K^{-1}$ and 72.4 $J{\cdot}kg^{-1}$, respectively, for a field change of 0–1 T. Lattice expansion and altered electronic interactions result in significant FM behavior and a low saturation field, which lead to a markedly enhanced MCE in the $EuTi_{0.875}Zr_{0.125}O_3$ compound [29]. Consequently, the values of $-\Delta S_M^{max}$ and the maximum adiabatic temperature change (ΔT_{ad}^{max}) reach 17.9 $J{\cdot}kg^{-1}{\cdot}K^{-1}$ and 6.1 K, respectively, under a field change of 0–1 T.

Previous studies not only provide effective inspiration for the development of high-performance $EuTiO_3$-based magnetocaloric materials but also lay a good foundation for the application of magnetic refrigeration technology. In this work, Nb and Zr were used to substitute part of the Ti in $EuTiO_3$ to obtain materials with a large low-field MCE. As expected, the obtained $EuTi_{0.8375}Nb_{0.0625}Zr_{0.1}O_3$ compound exhibited outstanding integrated magnetocaloric performance. The results of the magnetic refrigeration experiments further demonstrated that the compound is an excellent cryogenic magnetic refrigerant.

2 Experimental

2.1 Powder preparation

Polycrystalline $EuTi_{0.9375-x}Nb_{0.0625}Zr_xO_3$ (x = 0.075, 0.1, 0.125, and 0.15) compounds were synthesized via a solid-state reaction process. First, stoichiometric ratios of Eu_2O_3 (Aladdin, 99.99% purity), TiO_2 (Aladdin, 99.99% purity), Nb_2O_5 (Aladdin, 99.99% purity), and ZrO_2 (Aladdin, 99.99% purity) powders were ground for 6 h to homogenize and pulverize them well. The mixtures were then preheated in a muffle furnace at 1300 °C for 6 h to obtain single-phase $Eu_2Ti_2O_7$ precursors. Finally, the precursors were sintered in a tube furnace at 1300 °C for 6 h in a reducing atmosphere consisting of 5 vol% hydrogen and 95 vol% argon to obtain powder samples.

2.2 Magnetic refrigerant preparation

Considering the parameters of magnetic entropy change and refrigeration capacity, $EuTi_{0.8375}Nb_{0.0625}Zr_{0.1}O_3$ was selected as the magnetic refrigerant for refrigeration performance tests. To increase the heat transfer efficiency, the powder sample was processed into particles with a size of 200–300 μm. First, the powder sample was sufficiently pulverized via a vibration mill to obtain primary particles. An appropriate amount of polyvinyl alcohol solution with a concentration of 10 wt% was subsequently added to the primary particles as a binder. The mixture was subsequently processed into secondary particles via a drum pelletizer and then sintered at 1500 °C for 6 h under a protective atmosphere to obtain hardened particles. Finally, $EuTi_{0.8375}Nb_{0.0625}Zr_{0.1}O_3$ particles between 200 and 300 μm in size were obtained by sieving as a spare magnetic refrigerant.

2.3 Structure and property characterizations

Room-temperature X-ray diffraction (XRD) data of the powder samples were collected via an X-ray diffractometer (D8 Advance, Bruker). Cu Kα radiation at a wavelength of 1.5406 Å was used, with the voltage and current set at 40 kV and 40 mA, respectively. Fine XRD patterns in the 2θ range of 10°–80° were acquired with a step size of 2θ = 0.02° and a scanning speed of 1 s/step. The microstructure and elemental distribution of the compounds were characterized with a high-resolution field emission scanning electron microscope (SEM; JSM-IT800, JEOL) equipped with an energy dispersive spectrometer (EDS; Ultim Max 100, Oxford Instruments). Low-temperature XRD data were collected with a variable-temperature X-ray diffractometer (SmartLab, Rigaku). Magnetic measurements were performed on a magnetic property measurement system (MPMS; MPMS3, Quantum Design). Magnetization–temperature (M–T) curves were measured in both zero-field cooling (ZFC) and field cooling (FC) modes at an external magnetic field of 0.01 T. Isothermal magnetization (M–H) data were collected at a series of selected temperatures with magnetic fields ranging from 0 to 5 T. Specific heat measurements were performed on a physical property measurement system (PPMS; DynaCool, Quantum Design) with a heat capacity option.

2.4 Refrigeration performance tests

Refrigeration performance tests were performed on a self-developed hybrid GM magnetic refrigerator (KDE410M). Double Halbach permanent magnet arrays are coupled to a conventional GM refrigerator to provide a rotation magnetic field of up to 1.1 T. The regenerator is the core component of the refrigeration system and is generally filled with Pb and $HoCu_2$ microspheres as the upper and lower regenerative materials in conventional GM refrigerators, respectively. In this work, particles of self-developed $EuTi_{0.8375}Nb_{0.0625}Zr_{0.1}O_3$ were used to replace some of the commercial $HoCu_2$ microspheres to evaluate the practical cooling effect of the present material.

3 Results and discussion

3.1 Structural characterizations

Figure 1(a) and Fig. S1 in Electronic Supplementary Material (ESM) illustrate the room-temperature XRD patterns and the corresponding Rietveld refinements of the $Eu(Ti,Nb,Zr)O_3$ compounds. All the diffraction peaks match well with the Bragg diffraction peaks of cubic $EuTiO_3$ (space group $Pm3m$), without obvious additional diffraction peaks. A single high-purity cubic phase was obtained upon proper cosubstitution of Nb and Zr, which still maintains the crystal configuration of the parent compound, as shown in the inset in Fig. 1(a). In cubic $EuTiO_3$, Eu atoms occupy the eight vertices of a cubic unit cell, whereas Ti

atoms are located at the center of the cube and are surrounded by the oxygen octahedra. Here, Nb and Zr atoms partially replace the B-site Ti atoms in the lattice and form good solid solutions in the compounds. The lattice constant and cell volume increase almost linearly with increasing Zr substitution because the ionic radius of Zr is larger than the ionic radius of Ti [30], which further demonstrates a good solid solution for these compounds (Fig. 1(b)). The lattice constant of the $EuTi_{0.8375}Nb_{0.0625}Zr_{0.1}O_3$ compound (3.931 Å) is significantly greater than that of bulk $EuTiO_3$ (3.905 Å), accompanied by a volume increase of approximately 2%. In other words, Nb and Zr cosubstitution can cause significant lattice expansion without changing the crystal configuration, which has been proven to be conducive to the induction of FM behavior in $EuTiO_3$. As cryogenic magnetic refrigerants, their structural stability and performance at low temperatures should be of greater concern. On this basis, variable-temperature XRD measurements were performed on the $EuTi_{0.8375}Nb_{0.0625}Zr_{0.1}O_3$ compound in the vicinity of the liquid helium temperature. The XRD patterns at different temperatures are almost identical and highly compatible with the Bragg diffraction peaks of cubic $EuTiO_3$, as shown in Fig. S2 in the ESM, revealing good structural stability of the compound, which is conducive to practical applications.

Figure 2(a) presents a secondary electron SEM image of the surface microstructure of the block $EuTi_{0.8375}Nb_{0.0625}Zr_{0.1}O_3$ sample. The grains are irregularly polygonal with clear grain boundaries. The grain sizes are inhomogeneous and are distributed between approximately 10 and 50 μm. A few abnormally grown grains exist, possibly because Nb_2O_5 can act as a sintering aid and effectively promote the solid-phase sintering and grain growth processes. The surfaces of the grains are uneven and exhibit an obviously folded lamellar morphology, as illustrated in Fig. 2(b). To investigate the chemical composition and elemental distribution of the compounds, EDS mapping analysis was further performed for the $EuTi_{0.8375}Nb_{0.0625}Zr_{0.1}O_3$ sample. As depicted in Figs. 2(c)–2(g), Eu, Ti, Nb, Zr, and O are all uniformly distributed in the compound, with no visible compositional segregation or aggregation. The results demonstrate that the introduced Nb and Zr atoms successfully enter the lattice sites of Ti atoms and form a good substitutional solid solution, which is consistent with the XRD results. The chemical compositions obtained via EDS mapping are summarized in Table S1 in the ESM. The experimental proportions of the elements are close to the theoretical chemical composition of this compound.

3.2 Magnetic properties

Figure 3(a) and Figs. S3(a)–S3(c) in the ESM show the magnetization versus temperature (M-T) curves for the $Eu(Ti,Nb,Zr)O_3$ compounds collected in ZFC and FC modes at a magnetic field of 0.01 T. In a relatively high-temperature range, e.g., $T \geq 10$ K, the compounds exhibit a distinct paramagnetic (PM) state. In the liquid helium temperature range ($2\ K \leq T \leq 10\ K$), the compounds undergo a magnetic phase transition from paramagnetic to ferromagnetic (PM–FM) as the temperature decreases. The Curie temperatures (T_C) are established to be 5.0, 5.5, 5.5, and 6.0 K on the basis of first-order differentiation of the M-T curves, as illustrated in the insets. There is no significant separation/hysteresis between the ZFC and FC curves near the phase transition point, which facilitates practical applications.

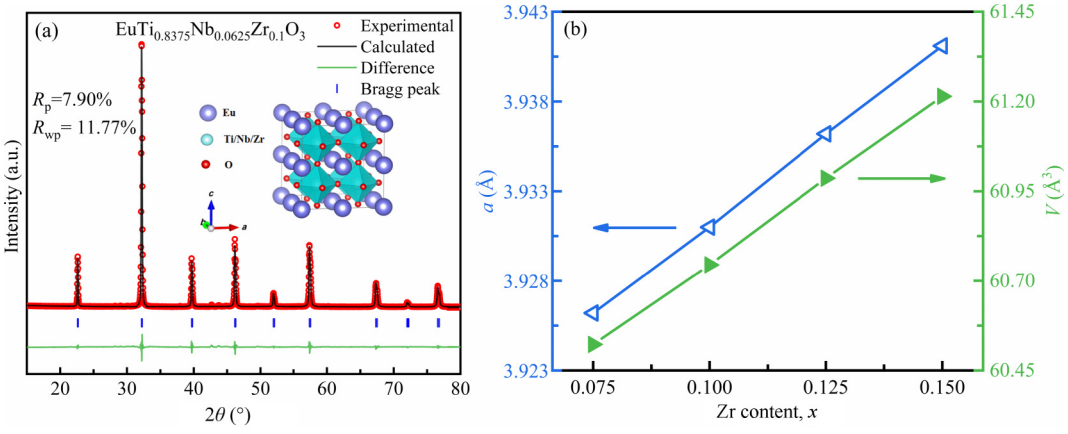

Fig. 1 (a) Room-temperature XRD pattern and Rietveld refinement of $EuTi_{0.8375}Nb_{0.0625}Zr_{0.1}O_3$ compound where the inset shows a schematic of crystal structure of this compound. (b) Room-temperature lattice constant and cell volume as a function of Zr content.

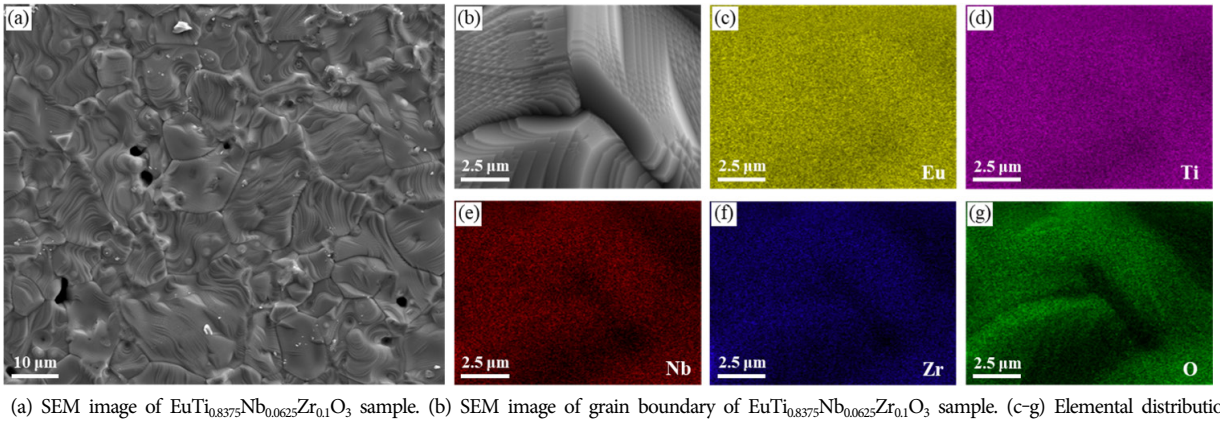

Fig. 2 (a) SEM image of $EuTi_{0.8375}Nb_{0.0625}Zr_{0.1}O_3$ sample. (b) SEM image of grain boundary of $EuTi_{0.8375}Nb_{0.0625}Zr_{0.1}O_3$ sample. (c–g) Elemental distributions of $EuTi_{0.8375}Nb_{0.0625}Zr_{0.1}O_3$ sample obtained via EDS mappings.

However, at lower temperatures, e.g., $T \leq 3.5$ K, significant cleavage occurs between the ZFC and FC curves, which is likely related to the glassy state induced by magnetic frustration behavior [31]. In the paramagnetic region, the inverse susceptibility (χ^{-1}) increases linearly with temperature and is in accordance with the Curie–Weiss law $\chi^{-1} = (T - \theta_{CW})/C$ where C is the Curie constant, as shown in Fig. 3(b) and Figs. S3(d)–S3(f) in the ESM. The experimental value of the Curie–Weiss temperature (θ_{CW}) of the $EuTi_{0.8375}Nb_{0.0625}Zr_{0.1}O_3$ compound is 3.62 K, and the effective magnetic moment (μ_{eff}) obtained from the Curie–Weiss fit is $7.95\mu_B$, which is very close to the theoretical value of $2\sqrt{J(J+1)}\mu_B = 7.94\mu_B$ where J is the total angular momentum quantum number [32]. The magnetization versus magnetic field (M-H) curves around T_C was measured to further investigate the magnetic phase transition and the magnetocaloric effect, as illustrated in Fig. 3(c) and Fig. S4 in the ESM. Below the phase transition point, M increases abruptly with increasing H at low magnetic fields (≤ 0.5 T) and then saturates rapidly, exhibiting significant FM behavior. At 2 K, the high degree of coincidence between the M-H curves for increasing and decreasing fields reveals the default of hysteresis, which is desirable in practical applications. For the four compounds investigated, M increases abruptly to $6\mu_B$/f.u. at 0.3 T and saturates in a magnetic field of 1 T, as shown in Fig. 3(d), which is very different from the AFM results for $EuTiO_3$. These results indicate that the cosubstitution of Nb and Zr drives the magnetic ground state transition of $EuTiO_3$ from AFM to FM, leading to a dominance of the FM state.

3.3 Magnetocaloric effect

The magnetic entropy change (ΔS_M) is a pivotal metric for assessing MCE of a magnetocaloric material, which is commonly estimated on the basis of magnetization data via the Maxwell equation (Eq. (1)) [33]:

$$\Delta S_M(T, \mu_0 H) = \int_{\mu_0 H_{initial}}^{\mu_0 H_{final}} \left(\frac{\partial M}{\partial T}\right)_{\mu_0 H} \mathrm{d}(\mu_0 H) \quad (1)$$

where $\mu_0 H$ and M represent the external magnetic field and the magnetization, respectively; $\mu_0 H_{initial}$ and $\mu_0 H_{final}$ are the initial and final magnetic fields, respectively. Because measured magnetization data are always discrete, an alternative format is usually used in numerical calculations, as shown in Eq. (2):

$$\Delta S_M(T, \mu_0 H) = \sum_i \frac{M_{i+1}(T_{i+1}, H_i) - M_i(T_i, H_i)}{T_{i+1} - T_i} \Delta H_i \quad (2)$$

where M, T, and H represent the magnetization, the temperature, and the magnetic field, respectively. The compound exhibits positive $-\Delta S_M$ values under a series of magnetic field changes from 0.5 to 5 T, with the maximum magnetic entropy change ($-\Delta S_M^{max}$) occurring around T_C, as illustrated in Fig. 4(a) and Figs. S6(a)–S6(c) in the ESM. Under low magnetic field changes, e.g., 0–0.5 and 0–1 T, no negative $-\Delta S_M$ occurs, which is consistent with the ferromagnetic nature of the compounds. The peak values of $-\Delta S_M$ of the compounds are 19.6 and 29.6 J·kg^{-1}·K^{-1} under field changes of 0–1 and 0–2 T, respectively. Figure 4(b) presents a comparison of $-\Delta S_M^{max}$ of the $Eu(Ti,Nb,Zr)O_3$ compounds for $\mu_0\Delta H$ = 0–1 T with those of several promising magnetic refrigerants operating near the liquid helium temperature [34–40]. Notably, the $Eu(Ti,Nb,Zr)O_3$ compounds exhibit a more pronounced magnetocaloric effect than the other

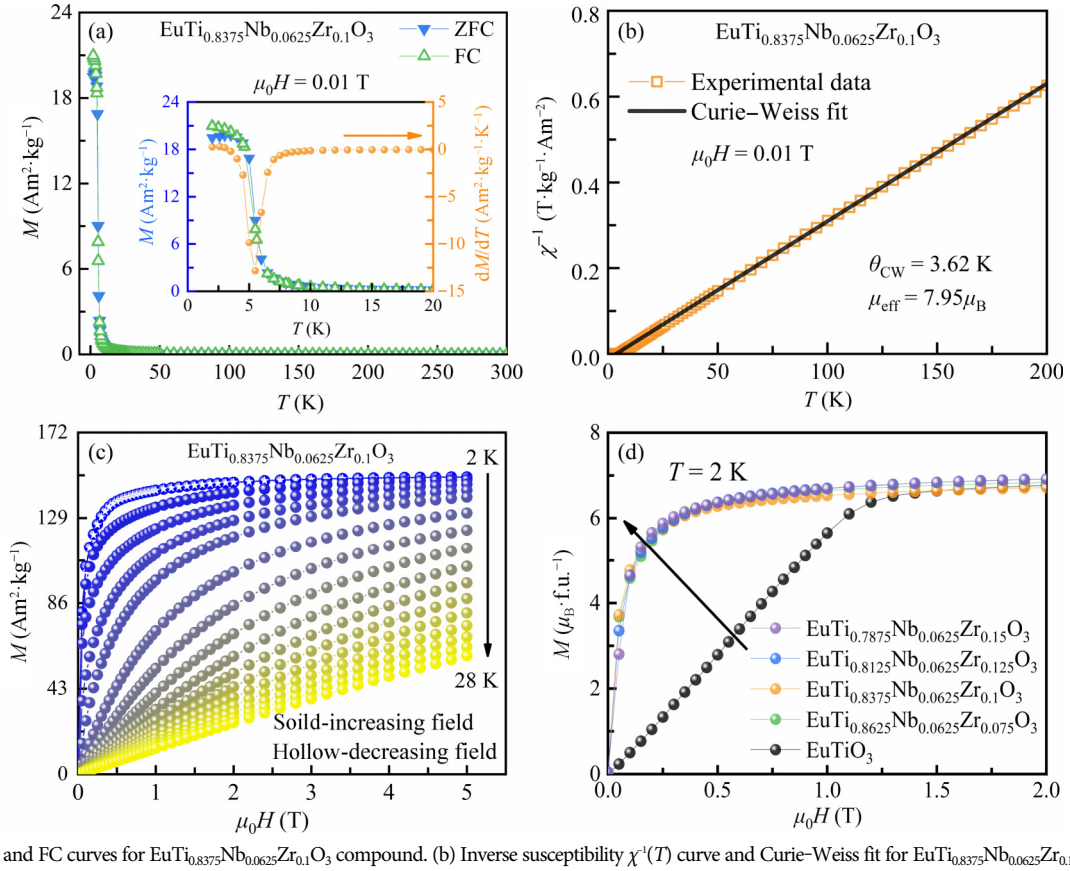

Fig. 3 (a) ZFC and FC curves for $EuTi_{0.8375}Nb_{0.0625}Zr_{0.1}O_3$ compound. (b) Inverse susceptibility $\chi^{-1}(T)$ curve and Curie–Weiss fit for $EuTi_{0.8375}Nb_{0.0625}Zr_{0.1}O_3$ compound. (c) Isothermal magnetization curves at different temperatures for $EuTi_{0.8375}Nb_{0.0625}Zr_{0.1}O_3$ compound. (d) Isothermal magnetization curves at 2 K for $Eu(Ti,Nb,Zr)O_3$ compounds with different Zr contents.

https://doi.org/10.26599/JAC.2024.9220992

compounds do, setting a new world record for the magnetic entropy change near the liquid helium temperature for a field change of 0–1 T. More astonishingly, the value of $-\Delta S_M^{max}$ reaches 11.8 J·kg^{-1}·K^{-1} under a field change of 0–0.5 T, comparable to or exceeding the values at 0–1 T for $EuTiO_3$ [23] and many competitive cryogenic materials, such as ErNiBC [34], TmZn [20], and TmCoSi [35].

Another crucial criterion for assessing MCE of magnetocaloric materials is refrigeration capacity (RC), which denotes the heat transfer between the hot and cold sides of the refrigeration cycle and can be estimated via Eq. (3):

$$RC = \int_{T_1}^{T_2} \left|\Delta S_M\left(T, \mu_0 H\right)\right| dT \quad (3)$$

where T_1 and T_2 are the temperatures of the cold and hot sides, respectively [41]. The peak values of RCs of the compounds are 87.6 and 173.6 J·kg^{-1} under field changes of 0–1 and 0–2 T, which are 165% and 64% greater than those of $EuTiO_3$, respectively. To evaluate the utility of these compounds more accurately, the temperature-averaged entropy change (TEC) is also investigated [42], which is defined as Eq. (4):

$$TEC(\Delta T) = \frac{1}{\Delta T}\max\left\{\int_{T_{mid}-\frac{\Delta T}{2}}^{T_{mid}+\frac{\Delta T}{2}} \left|\Delta S_M\left(T\right)\right| dT\right\} \quad (4)$$

where ΔT refers to a given temperature range, and T_{mid} refers to the temperature that maximizes TEC(ΔT). TEC(5) of these four compounds reaches impressive values of 15.5, 15.2, 15.0, and 14.6 J·kg^{-1}·K^{-1}, respectively, which demonstrates that these compounds could be excellent magnetic refrigerants operating in the vicinity of the liquid helium temperature. Figure S6(d) in the ESM shows the variation in the values of $-\Delta S_M^{max}$, TEC(5), and RC with respect to the Zr content for a field change of 0-1 T. Although the values of $-\Delta S_M^{max}$ and TEC(5) decrease progressively with increasing Zr content, RC increases gradually as the Zr content increases. The values of $-\Delta S_M^{max}$, TEC(5), and RC of the $EuTi_{0.8375}Nb_{0.0625}Zr_{0.1}O_3$ compound are 18.8 J·kg^{-1}·K^{-1}, 15.2 J·kg^{-1}·K^{-1}, and 83.3 J·kg^{-1}, respectively, indicating outstanding magnetocaloric performance.

The adiabatic temperature change (ΔT_{ad}) is a vital parameter for directly evaluating the MCE of magnetocaloric materials and can be calculated from Eq. (5) on the basis of specific heat data:

$$\Delta T_{ad}\left(T, \Delta H\right) = \left[T\left(S, H_F\right) - T(S, H_I)\right] \quad (5)$$

where H_F and H_I represent the final and initial magnetic fields, respectively. Figure 4(c) shows the temperature dependence of the specific heat of the $EuTi_{0.8375}Nb_{0.0625}Zr_{0.1}O_3$ compound. A sharp inflection can be observed in the zero-field specific heat curve, indicating a phase transition at 3.9 K, which is markedly lower than T_C determined from the M-T curve. Under an applied magnetic field, the specific heat curve gradually becomes broader and shorter, which may be related to the Schottky effect [43]. Figure 4(d) presents the temperature dependence of ΔT_{ad} of the compound under field changes of 0–0.5 and 0–1 T. The peak values of ΔT_{ad} (ΔT_{ad}^{max}) for the $EuTi_{0.8375}Nb_{0.0625}Zr_{0.1}O_3$ compound are calculated as 2.5 and 5.5 K under field changes of 0–0.5 and 0–1 T, respectively. These values are somewhat improved compared with those of $EuTiO_3$. Notably, the value of ΔT_{ad}^{max} for $\mu_0\Delta H$= 0–0.5 T is comparable to or even greater than those of typical magnetocaloric materials such as $ErMn_2Si_2$ [36], $ErNi_2$ [44], and $DyVO_4$ under a field change of 0–1 T [45]. On the basis of overall considerations of the MCE parameters, including $-\Delta S_M^{max}$, RC, and ΔT_{ad}^{max}, the $EuTi_{0.8375}Nb_{0.0625}Zr_{0.1}O_3$ compound exhibits remarkable competitiveness among the well-known magnetic refrigerants in the liquid helium temperature range. In other words, the outstanding low-field MCE performance of the

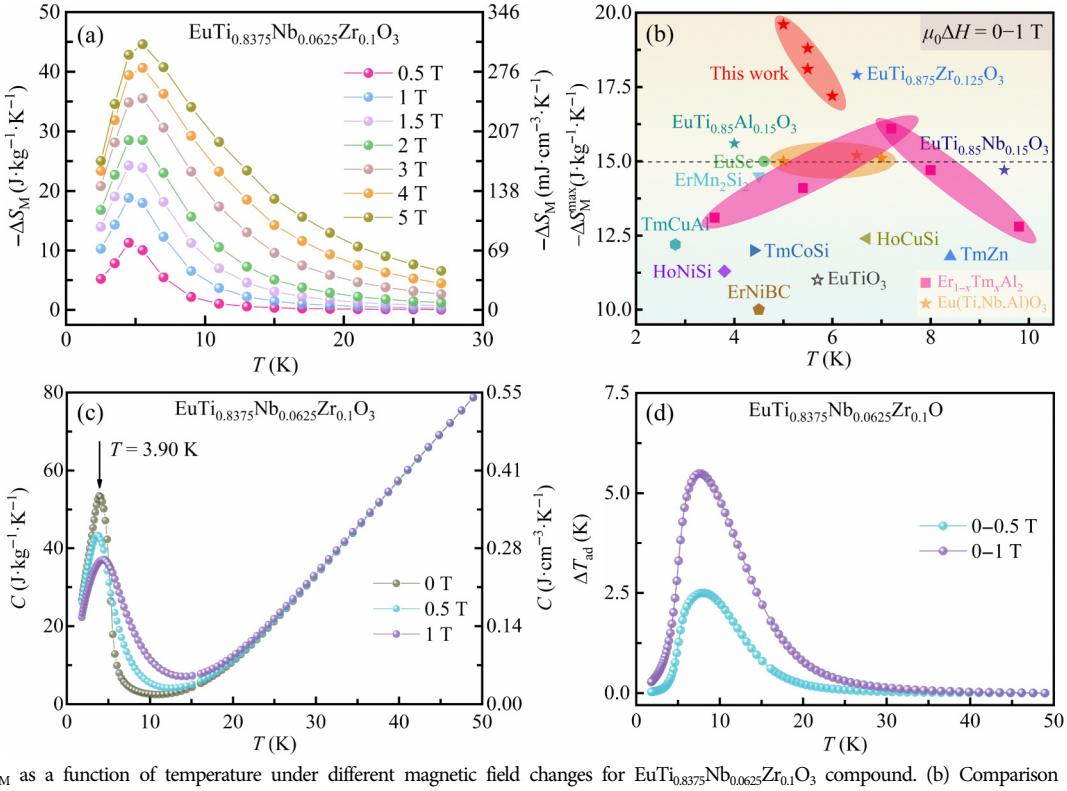

Fig. 4 (a) -ΔS_M as a function of temperature under different magnetic field changes for $EuTi_{0.8375}Nb_{0.0625}Zr_{0.1}O_3$ compound. (b) Comparison of $-\Delta S_M^{max}$ of Eu(Ti,Nb,Zr)O_3 compounds for $\mu_0\Delta H$ = 0–1 T with several promising magnetic refrigerants operating near the liquid helium temperature. (c) Temperature dependencies of specific heat at different magnetic fields for $EuTi_{0.8375}Nb_{0.0625}Zr_{0.1}O_3$ compound. (d) ΔT_{ad} as a function of temperature for $EuTi_{0.8375}Nb_{0.0625}Zr_{0.1}O_3$ compound under field changes of 0–0.5 and 0–1 T, respectively.

$EuTi_{0.8375}Nb_{0.0625}Zr_{0.1}O_3$ compound, which originates from its FM behavior and low saturation magnetic field, makes it an excellent magnetic refrigerant operating in the vicinity of the liquid helium temperature.

3.4 Order of magnetic phase transition

The type of magnetic phase transition of magnetocaloric materials has a significant influence on their practical applications. In general, second-order phase transition (SOPT) materials are preferred because of their negligible hysteresis and better thermomagnetic reversibility [33,36]. Therefore, the order of magnetic phase transition (MPT) of the $Eu(Ti,Nb,Zr)O_3$ compounds was further investigated via different methods prior to their utilization in a refrigerator. Figure 5(a) and Fig. S7(a)-S7(c) in the ESM present the Arrott plots of the compounds, and the monotonically positive slope indicates their second-order characteristics according to Banerjee's criterion [46].

The MPT order of the compounds was subsequently analyzed according to the master curve criterion proposed by Franco *et al.* [47], on the basis of which the rescaled $\Delta S'-\theta$ curves of SOPT materials at various field changes overlap into a master curve. Here, the rescaled $\Delta S'-\theta$ curves are obtained from the $-\Delta S_M-T$ curves via Eqs. (6) and (7):

$$\Delta S'\left(T,\mu_0 H_{\max}\right)=\frac{\Delta S_M\left(T,\mu_0 H_{\max}\right)}{\Delta S_M^{\max}\left(\mu_0 H_{\max}\right)} \tag{6}$$

$$\theta=\begin{cases}-\left(T-T_C\right)/\left(T_{r1}-T_C\right), T\le T_C\\ \left(T-T_C\right)/\left(T_{r2}-T_C\right), \quad T>T_C\end{cases} \tag{7}$$

where T_{r1} and T_{r2} represent two reference temperatures typically chosen as those corresponding to $1/2\Delta S_M^{\max}$. As shown in Figs. 5(b) and Figs. S7(d)-S7(f) in the ESM, the rescaled curves overlap well with each other, which further demonstrates SOPT characteristics of the $Eu(Ti,Nb,Zr)O_3$ compounds.

In addition, the exponent n calculated from Eq. (8) can be used as a quantitative criterion for determining the order of a magnetic phase transition [48]:

$$n\left(T,H\right)=\frac{\mathrm{d}\ln\left|\Delta S_M\right|}{\mathrm{d}\ln H} \tag{8}$$

Figure 5(c) and Figs. S7(g)-S7(i) in the ESM show the variation in n with temperature for the $Eu(Ti,Nb,Zr)O_3$ compounds. There is no sign of a first-order magnetic phase transition (i.e., $n > 2$) over the range of temperatures tested under different magnetic field changes, which further demonstrates that the compound is an SOPT material. The results show that the cosubstitution of Nb and Zr changes the order of MPT of $EuTiO_3$ from a first-order phase transition to a second-order phase transition, which makes the compound more favorable for practical applications.

3.5 Magnetic refrigeration performance

Figure 6(a) displays the GM/magnetic hybrid refrigerator model KDE410M used in this study. Pb microspheres, $HoCu_2$ microspheres, and $EuTi_{0.8375}Nb_{0.0625}Zr_{0.1}O_3$ particles were used as the regenerative fillers of the multilayer active magnetic regenerator, as shown in Fig. 6(b) and Table S3 in the ESM. The cooling power first increased with increasing $EuTi_{0.8375}Nb_{0.0625}Zr_{0.1}O_3$ particles, peaked at 30 g, and then decreased rapidly, as depicted in Fig. 6(c) and Fig. S8 in the ESM. When 30 g of $EuTi_{0.8375}Nb_{0.0625}Zr_{0.1}O_3$ was used to replace 48.1 g of $HoCu_2$, the cooling power at 4.2 K and 0.5 Hz reached 0.82 W in the absence of an external magnetic field, as shown in Fig. 6(d), which is 32% greater than that in the pure GM/$HoCu_2$ mode. At an applied magnetic field of 1.1 T, the value reached 0.94 W, accompanied by a further improvement of 15% in cooling power. The results show that the cooling power in the GM/magnetic hybrid refrigeration mode is 52% greater than that in the pure GM/$HoCu_2$ mode at 4.2 K and 0.5 Hz. Figure 6(e) shows the variation in cooling efficiency with frequency in different modes at a temperature of 4.2 K. The cooling efficiency of the GM/magnetic hybrid refrigerator is more than 40% greater than that of the pure GM/$HoCu_2$ refrigerator. The results further demonstrate that the $EuTi_{0.8375}Nb_{0.0625}Zr_{0.1}O_3$ compound is an excellent cryogenic magnetic refrigerant, which is promising for application in liquid helium refrigeration.

The conventional GM refrigerator allows cooling via adiabatic venting through continuous Simon expansion. As the temperature decreases to near the liquid helium temperature, helium tends to be increasingly similar to a liquid, accompanied by a sharp increase in the specific heat capacity [49]. Moreover, the specific heat of regenerative materials (e.g., $HoCu_2$) plummets, which results in a rapid decrease in the cooling power. In the presence of a small amount of the $EuTi_{0.8375}Nb_{0.0625}Zr_{0.1}O_3$ refrigerant, the remarkable increase in the cooling power without an external magnetic field is attributed to the significantly greater specific heat of $EuTi_{0.8375}Nb_{0.0625}Zr_{0.1}O_3$ than that of $HoCu_2$ below 5 K (Fig. S9 in the ESM) [50]. The cooling power further increases in the presence of an external magnetic field of 1.1 T, which benefits from the large MCEs of this refrigerant at low magnetic fields. In hybrid refrigeration mode, $EuTi_{0.8375}Nb_{0.0625}Zr_{0.1}O_3$ acts not only as a magnetic refrigerant but also as an excellent heat regeneration material, and the combination of these two effects significantly improves the refrigeration performance. However, the cooling

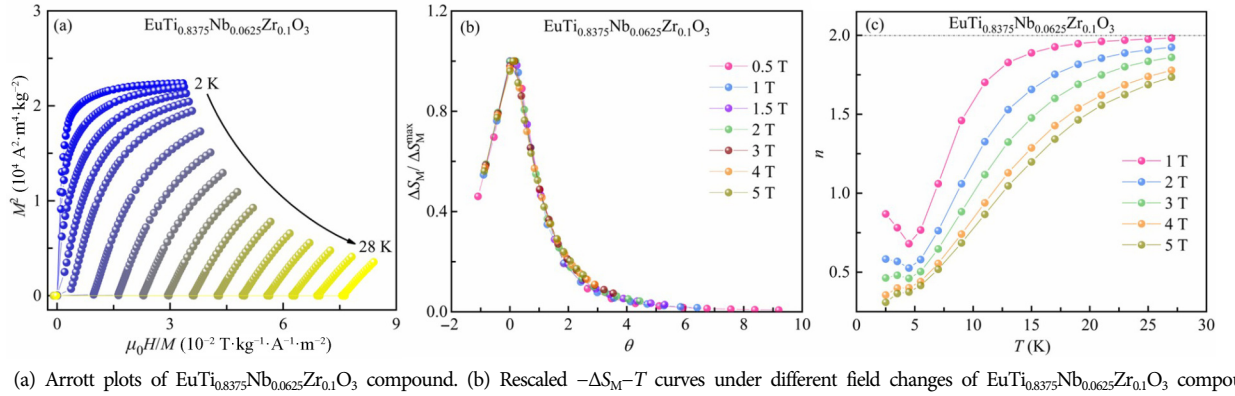

Fig. 5 (a) Arrott plots of $EuTi_{0.8375}Nb_{0.0625}Zr_{0.1}O_3$ compound. (b) Rescaled $-\Delta S_M-T$ curves under different field changes of $EuTi_{0.8375}Nb_{0.0625}Zr_{0.1}O_3$ compound. (c) Temperature dependencies of exponent n for $EuTi_{0.8375}Nb_{0.0625}Zr_{0.1}O_3$ compound.

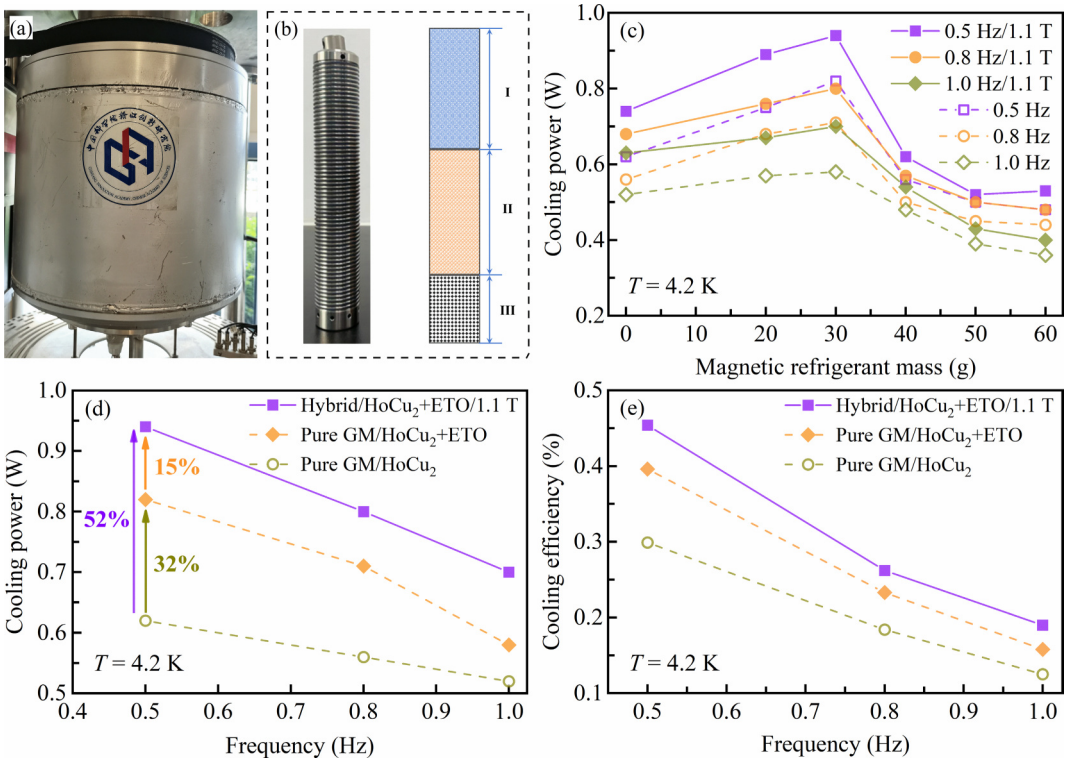

Fig. 6 (a) Photo of GM/magnetic hybrid refrigerator. (b) Photograph of magnetic regenerator and schematic diagram of multilayer active magnetic regenerator (I–Pb microspheres, II–$HoCu_2$ microspheres, III–$EuTi_{0.8375}Nb_{0.0625}Zr_{0.1}O_3$ particles). (c) Cooling power as a function of mass of $EuTi_{0.8375}Nb_{0.0625}Zr_{0.1}O_3$ particles at 4.2 K. (d) Cooling power variation with frequency at 4.2 K with 30 g of magnetic refrigerant charge. (e) Cooling efficiency as a function of frequency for different cooling modes at temperature of 4.2 K.

power of the hybrid refrigerator instead decreases rapidly as the charge of the magnetic refrigerant exceeds 30 g, which is probably due to the markedly lower density of $EuTi_{0.8375}Nb_{0.0625}Zr_{0.1}O_3$ than that of $HoCu_2$. Since the total volume of the regenerator remains unchanged, the mass of $HoCu_2$ decreases rapidly when the mass of $EuTi_{0.8375}Nb_{0.0625}Zr_{0.1}O_3$ increases, leading to a significant decrease in the total mass of the fillers and thus in the cooling power.

4 Conclusions

In summary, a series of $EuTiO_3$-based polycrystalline compounds with large low-field MCEs were synthesized via a solid-state reaction process. Cosubstitution of niobium and zirconium results in a dominance of ferromagnetic interactions in the compounds and significantly reduces the saturation magnetic field. Consequently, the peaks of $-\Delta S_M$, RC, and ΔT_{ad} reach remarkable values of 19.6 $J{\cdot}kg^{-1}{\cdot}K^{-1}$, 87.6 $J{\cdot}kg^{-1}$, and 5.5 K, respectively, under field changes of 0–1 T. More surprisingly, the value of $-\Delta S_M^{max}$ reaches 11.8 $J{\cdot}kg^{-1}{\cdot}K^{-1}$ for a field change of 0–0.5 T, comparable to or exceeding the values at 0–1 T for many competitive cryogenic magnetic refrigeration materials. The magnetic refrigeration performance of $EuTi_{0.8375}Nb_{0.0625}Zr_{0.1}O_3$ was subsequently investigated on a GM/magnetic hybrid refrigerator. When 48.1 g of commercial $HoCu_2$ microspheres are replaced with 30 g of $EuTi_{0.8375}Nb_{0.0625}Zr_{0.1}O_3$ particles, the cooling power and cooling efficiency in hybrid refrigeration mode can be improved by more than 50% and 40%, respectively, compared with those in pure GM/$HoCu_2$ refrigeration mode. The results demonstrate that this series of compounds are excellent magnetic refrigerants operating in the vicinity of the liquid helium temperature.

Acknowledgements

This work was supported by the National Key R&D Program of China (Grant No. 2021YFB3501204), the National Science Foundation for Excellent Young Scholars (Grant No. 52222107), and the National Natural Science Foundation of China (Grant No. 52171195).

Declaration of competing interest

The authors have no competing interests to declare that are relevant to the content of this article.

Electronic Supplementary Material

Supplementary material is available in the online version of this article at https://doi.org/10.26599/JAC.2024.9220992.

References

[1] Xiang JS, Zhang CD, Gao Y, *et al.* Giant magnetocaloric effect in spin supersolid candidate $Na_2BaCo(PO_4)_2$. *Nature* 2024, **625**: 270–275.

[2] Wang GP, Li JG, Wei LJ, *et al.* Design and test of a liquid helium cryogenic system for the cooling of a superconductive single-flux-quantum circuit chip. *Cryogenics* 2021, **114**: 103242.

[3] Vshivkov AY, Delkov AV, Kishkin AA, *et al.* Results of ground-based testing of passive heat protection for liquid helium temperature spacecraft devices. *Chem Petrol Eng* 2019, **55**: 306–311.

[4] Terada N, Mamiya H. High-efficiency magnetic refrigeration using holmium. *Nat Commun* 2021, **12**: 1212.

[5] He YJ, Cao C, Wu J, *et al.* Investigations on coupling between performance and external operational conditons for a simiconductor refrigeration system. *Int J Refrig* 2020, **109**: 172–179.

[6] Niu X, Jian XD, Chen XY, *et al.* Enhanced electrocaloric effect at room temperature in Mn^{2+} doped lead-free (BaSr)TiO_3 ceramics via a direct measurement. *J Adv Ceram* 2021, **10**: 482–492.

[7] Klinar K, Law JY, Franco V, *et al.* Perspectives and energy applications of magnetocaloric, pyromagnetic, electrocaloric, and pyroelectric materials. *Adv Energy Mater* 2024, **14**: 2401739.
[8] Wang X, Xu JY, Wu ZH, *et al.* A thermoacoustic refrigerator with multiple-bypass expansion cooling configuration for natural gas liquefaction. *Appl Energy* 2022, **313**: 118780.
[9] Hamad MA. Magnetocaloric effect in $La_{1-x}Ce_xMnO_3$. *J Adv Ceram* 2015, **4**: 206–210.
[10] Zhang YK, Hao WX, Hu CL, *et al.* Rare-earth-free $Mn_{30}Fe_{20-x}Cu_xAl_{50}$ magnetocaloric materials with stable cubic CsCl-type structure for room-temperature refrigeration. *Adv Funct Mater* 2023, **33**: 2310047.
[11] Lin Y, Wang J, Dai W, *et al.* A full solid-state conceptual magnetocaloric refrigerator based on hybrid regeneration. *Innovation* 2024, **5**: 100645.
[12] Zhong H, Song YZ, Long FX, *et al.* Design of excellent mechanical performances and magnetic refrigeration via *in situ* forming dual-phase alloys. *Adv Mater* 2024, **36**: 2402046.
[13] Zhang YK, Hao WX, Lin JL, *et al.* Geometrically frustrated $Gd_2Ti_2O_7$ oxide: A comprehensive exploration of structural, magnetic, and magnetocaloric properties for cryogenic magnetic cooling applications. *Acta Mater* 2024, **272**: 119946.
[14] Zhang YK, Na YZ, Hao WX, *et al.* Enhanced cryogenic magnetocaloric effect from 4f–3d exchange interaction in B-site ordered Gd_2CuTiO_6 double perovskite oxide. *Adv Funct Mater* 2024: 2409061.
[15] Yayama H, Hatta Y, Tomokiyo A. Hybrid cryogenic refrigerator combining magnetic- and gas-cooling system. *Physica B* 2000, **284**: 2016–2017.
[16] Shen J, Gao XQ, Li K, *et al.* Experimental research on a 4 K hybrid refrigerator combining GM gas refrigeration effect with magnetic refrigeration effect. *Cryogenics* 2019, **99**: 99–104.
[17] Li K, Guo XH, Dai W, *et al.* Numerical simulation of a low temperature hybrid refrigerator combining GM gas expansion refrigeration with magnetic refrigeration. *Cryogenics* 2021, **113**: 103235.
[18] Zheng WS, Shen J, Li ZX, *et al.* Performance improvement of a 4 K GM/magnetic hybrid refrigerator with a new magnetic regenerator. *Appl Therm Eng* 2023, **226**: 120272.
[19] Mo ZJ, Shen J, Yan LQ, *et al.* Low-field induced giant magnetocaloric effect in TmCuAl compound. *Appl Phys Lett* 2013, **102**: 192407.
[20] Li LW, Yuan Y, Zhang YK, *et al.* Giant low field magnetocaloric effect and field-induced metamagnetic transition in TmZn. *Appl Phys Lett* 2015, **107**: 132401.
[21] Yang SX, Zheng XQ, Wang DS, *et al.* Giant low-field magnetocaloric effect in ferromagnetically ordered $Er_{1-x}Tm_xAl_2$ ($0 \le x \le 1$) compounds. *J Mater Sci Technol* 2023, **146**: 168–176.
[22] Mo ZJ, Liu QY, Hao WX, *et al.* Magnetic properties and large low-field cryogenic magnetocaloric effect in the divalent europium borate $Eu_2B_2O_5$ compound. *Mater Today Phys* 2024, **41**: 101351.
[23] Mo ZJ, Shen J, Li L, *et al.* Observation of giant magnetocaloric effect in $EuTiO_3$. *Mater Lett* 2015, **158**: 282–284.
[24] Akamatsu H, Kumagai Y, Oba F, *et al.* Antiferromagnetic superexchange via 3d states of titanium in $EuTiO_3$ as seen from hybrid Hartree–Fock density functional calculations. *Phys Rev B* 2011, **83**: 214421.
[25] Zhao R, Ji YD, Yang C, *et al.* Origin of unexpected lattice expansion and ferromagnetism in epitaxial $EuTiO_{3-\delta}$ thin films. *Ceram Int* 2020, **46**: 19990–19995.
[26] Xu S, Gu YN, Wu XS. Structural, electronic and magnetic properties of a ferromagnetic metal: Nb-doped $EuTiO_3$. *J Magn Magn Mater* 2020, **497**: 166077.
[27] Lee JH, Fang L, Vlahos E, *et al.* A strong ferroelectric ferromagnet created by means of spin-lattice coupling. *Nature* 2010, **466**: 954–958.
[28] Roy S, Khan N, Mandal P. Giant low-field magnetocaloric effect in single-crystalline $EuTi_{0.85}Nb_{0.15}O_3$. *APL Mater* 2016, **4**: 026102.
[29] Xie HC, Lv XD, Mo ZJ, *et al.* Tailoring the cryogenic magnetism and magnetocaloric effect from Zr substitution in $EuTiO_3$ perovskite. *J Mater Sci Technol* 2024, **193**: 90–97.
[30] Akamatsu H, Fujita K, Hayashi H, *et al.* Crystal and electronic structure and magnetic properties of divalent europium perovskite oxides $EuMO_3$ (M = Ti, Zr, and Hf): Experimental and first-principles approaches. *Inorg Chem* 2012, **51**: 4560–4567.
[31] Wei T, Song QG, Zhou QJ, *et al.* Cr-doping induced ferromagnetic behavior in antiferromagnetic $EuTiO_3$ nanoparticles. *Appl Surf Sci* 2011, **258**: 599–603.
[32] Midya A, Mandal P, Rubi K, *et al.* Large adiabatic temperature and magnetic entropy changes in $EuTiO_3$. *Phys Rev B* 2016, **93**: 094422.
[33] Shen BG, Sun JR, Hu FX, *et al.* Recent progress in exploring magnetocaloric materials. *Adv Mater* 2009, **21**: 4545–4564.
[34] Li LW, Kadonaga M, Huo DX, *et al.* Low field giant magnetocaloric effect in *R*NiBC (*R* = Er and Gd) and enhanced refrigerant capacity in its composite materials. *Appl Phys Lett* 2012, **101**: 122401.
[35] Xu JW, Zheng XQ, Yang SX, *et al.* Giant low field magnetocaloric effect in TmCoSi and TmCuSi compounds. *J Alloys Compd* 2020, **843**: 155930.
[36] Li LW, Nishimura K, Hutchison WD, *et al.* Giant reversible magnetocaloric effect in $ErMn_2Si_2$ compound with a second order magnetic phase transition. *Appl Phys Lett* 2012, **100**: 152403.
[37] Li DX, Yamamura T, Nimori S, *et al.* Giant and isotropic low temperature magnetocaloric effect in magnetic semiconductor EuSe. *Appl Phys Lett* 2013, **102**: 152409.
[38] Zhang W, Mo ZJ, Jiang WH, *et al.* Giant low-field magnetic refrigeration in $EuTi_{1-x}Al_xO_3$ (x = 0.05, 0.1 and 0.15) compounds. *J Magn Magn Mater* 2019, **492**: 165684.
[39] Hao JZ, Hu FX, Zhou HB, *et al.* Large enhancement of magnetocaloric effect driven by hydrostatic pressure in HoCuSi compound. *Scripta Mater* 2020, **186**: 84–88.
[40] Zhang H, Xing CF, Zhou H, *et al.* Giant anisotropic magnetocaloric effect by coherent orientation of crystallographic texture and rare-earth ion moments in HoNiSi ploycrystal. *Acta Mater* 2020, **193**: 210–220.
[41] Franco V, Blázquez JS, Ipus JJ, *et al.* Magnetocaloric effect: From materials research to refrigeration devices. *Prog Mater Sci* 2018, **93**: 112–232.
[42] Griffith LD, Mudryk Y, Slaughter J, *et al.* Material-based figure of merit for caloric materials. *J Appl Phys* 2018, **123**: 034902.
[43] Das M, Roy S, Mandal P. Giant reversible magnetocaloric effect in a multiferroic $GdFeO_3$ single crystal. *Phys Rev B* 2017, **96**: 174405.
[44] Ćwik J, Koshkid'ko Y, Nenkov K, *et al.* Structural, magnetic and magnetocaloric properties of $HoNi_2$ and $ErNi_2$ compounds ordered at low temperatures. *J Alloys Compd* 2018, **735**: 1088–1095.
[45] Midya A, Khan N, Bhoi D, *et al.* Giant magnetocaloric effect in antiferromagnetic $DyVO_4$ compound. *Phys B Condens Matter* 2014, **448**: 43–45.
[46] Banerjee BK. On a generalised approach to first and second order magnetic transitions. *Phys Lett* 1964, **12**: 16–17.
[47] Franco V, Blázquez JS, Conde A. Field dependence of the magnetocaloric effect in materials with a second order phase transition: A master curve for the magnetic entropy change. *Appl Phys Lett* 2006, **89**: 222512.
[48] Law JY, Franco V, Moreno-Ramírez LM, *et al.* A quantitative criterion for determining the order of magnetic phase transitions using the magnetocaloric effect. *Nat Commun* 2018, **9**: 2680.
[49] Hong CS, Xu XD. On the thermodynamic cycle of the low temperature GM refrigerator. *Cryogenics* 1994, **34**: 183–186.
[50] Zhi XQ, Cao RF, Huang C, *et al.* Feasibility analysis of $HoCu_2$ and Gd_2O_2S as regenerative materials around 4–20K. *Appl Therm Eng* 2021, **192**: 116921.